ACS Sustainable Chemistry & Engineering

pubs.acs.org/journal/ascecg

Research Article

Investigation of Carbonation Kinetics in Carbonated Cementitious Materials by Reactive Molecular Dynamics Simulations

Ling Qin, Qijie Xie, Jiuwen Bao, Gaurav Sant, Tiefeng Chen, Peng Zhang, Ditao Niu,* Xiaojian Gao,* and Mathieu Bauchy*

Cite This: *ACS Sustainable Chem. Eng.* 2024, 12, 10075−10088

Read Online

ACCESS | Metrics & More | Article Recommendations

ABSTRACT: Calcium carbonate ($CaCO_3$) precipitation plays a significant role during the carbon capture process; however, the mechanism is still only partially understood. Understanding the atomic-level carbonation mechanism of cementitious materials can promote the mineralization capture, immobilization, and utilization of carbon dioxide, as well as the improvement of carbonated cementitious materials' performance. Therefore, based on molecular dynamics simulations, this paper investigates the effect of Si/Al concentrations in cementitious materials on carbonation kinetics. We first verify the force field used in this paper. Then, we analyze the network connectivity evolution, the number and size of the carbonate cluster during gelation, the polymerization rate, and the activation energy. Finally, in order to reveal the reasons that caused the evolution of polymerization rate and activation energy, we analyze the local stress and charge of atoms. Results show that the Ca−Oc bond number and carbonate cluster size increase with the decrease of the Si/Al concentration and the increase of temperature, leading to the higher amorphous calcium carbonate gel polymerization degree. The local stress of each atom in the system is the driving force of the gelation transition. The presence of Si and Al components increases the atom's local stress and average charge, thus causing the increase of the energy barrier of $CaCO_3$ polymerization and the activation energy of carbonation.

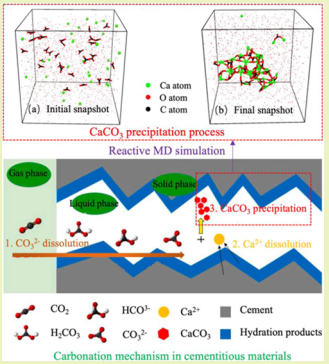

KEYWORDS: *molecular dynamics simulation, carbonation kinetics, cementitious material, carbonation curing, carbon capture*

1. INTRODUCTION

The environmental impacts related to energy use have received widespread attention since the 1990s due to the phenomenon of global climate change.[1] A large amount of greenhouse gases is released in the process of energy use. Among these greenhouse gases, carbon dioxide (CO_2) is the main contributor to the greenhouse effect. Cement concrete is the most widely used material for building and other infrastructure in the world due to its low cost and the widespread geographical abundance of its raw materials.[2−5] However, the cement and concrete industry is the main industrial production source of carbon dioxide emissions. Portland cement (OPC), as the main cementitious material, accounts for about 10% of the total concrete mass.[6] According to a report, the global OPC production is about 4.2 billion tons per year.[3] Cement production is a high energy consumption and CO_2 release process, which accounts for about 3% of the primary energy use and nearly 9% of the global anthropogenic carbon dioxide emissions.[5] There are three factors resulting in such carbon dioxide emissions: (1) thermal decomposition of limestone during the Portland clinker production process; (2) burning of fuel required to obtain the necessary temperature (about 1450 °C) for the synthesis of the cement clinker; and (3) supply of electricity during the cement clinker calcination and grinding process.[7,8] Specifically, about 0.9 tons of CO_2 is emitted and about 3.4 GJ of heat energy is consumed per ton of OPC produced.[9,10] Thus, it is essential to decrease the cement carbon footprint.

Cement concrete is a calcium-containing material, so it can capture and store carbon dioxide itself mainly via three ways: (1) carbonating the raw materials of cement concrete before concrete preparation, such as waste cementitious materials and recycled aggregate;[11−13] (2) carbonating the fresh concrete during the mixing period of raw materials;[14−16] and (3) accelerated carbonation curing of cement concrete.[17−19] Direct carbonation of the recycled aggregate can improve its density, reduce water absorption, and improve mechanical properties.[11−13] Carbonation curing as well as fresh concrete carbonation during its mixing can also improve the performance of cement concrete.[20] Among these three methods, carbonation curing has the highest carbon sequestration efficiency, which is about 3−4 times that of the other two methods.[21] As a result, carbonation curing has become the most commonly used way and has attracted more and more attention. During carbonation

Received: November 29, 2023
Revised: June 8, 2024
Accepted: June 10, 2024
Published: June 24, 2024

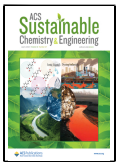

Table 1. Initial Components of the Simulation System

group	Si/Ca ratio (%)	Al/Ca ratio (%)	Ca	CO_3	H_2O	$Si(OH)_4$	$Al(OH)_3$
1	0	0	30	30	1000	0	0
2	1	0	30	30	1000	30	0
3	2	0	30	30	1000	60	0
4	3	0	30	30	1000	90	0
5	4	0	30	30	1000	120	0
6	1	0.1	30	30	1000	30	3
7	1	0.2	30	30	1000	30	6
8	1	0.3	30	30	1000	30	9
9	1	0.4	30	30	1000	30	12

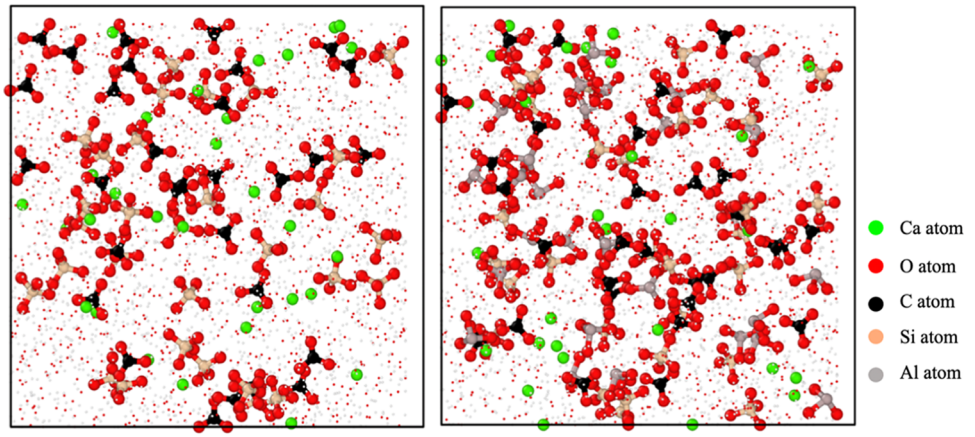

Figure 1. Initial configuration snapshots of the simulation systems.

curing, which occurs in early-age cement concrete, CO_2 reacts with cement clinker and hydration producers to form calcium carbonate ($CaCO_3$) as per the following reactions[22,23]

$$x(3CaO{\cdot}SiO_2) + yCO_2 + zH_2O \rightarrow (3x - y)CaO{\cdot}xSiO_2{\cdot}zH_2O + yCaCO_3 \quad (1)$$

$$x(2CaO{\cdot}SiO_2) + yCO_2 + zH_2O \rightarrow (2x - y)CaO{\cdot}xSiO_2{\cdot}zH_2O + yCaCO_3 \quad (2)$$

$$3CaO{\cdot}2SiO_2{\cdot}3H_2O + 3CO_2 \rightarrow 3CaCO_3{\cdot}2SiO_2{\cdot}3H_2O \quad (3)$$

$$Ca(OH)_2 + CO_2 \rightarrow CaCO_3 + H_2O \quad (4)$$

The formed $CaCO_3$ can lead to the improvement of performance and durability of cement concrete because of the improvement of the pore structure.[24−26] Besides the carbonation of cement concrete, some research focused on the direct carbonation of mineral admixtures such as coal fly ash to achieve clinkering-free cementation.[5] No matter it is the carbonation of cement concrete or the direct carbonation of the mineral admixture, the carbonation reaction was carried out through a solution-precipitation process, where oxygen from water molecules adsorbs onto dissolved Ca^{2+}, and interaction with CO_3^{2-} to precipitate amorphous calcium carbonate (ACC) gel. Finally, the amorphous precursor was dried and crystallized to form crystalline $CaCO_3$.[27,28] Therefore, understanding the amorphous calcium carbonate gel formation mechanism is significant because it is the precursor of crystalline carbonate phases. Macroscopic characteristics of carbonated cement have been studied extensively; however, few studies about the atomical-scale mechanism of cementitious materials' carbonation were carried out. There have been attempts to use molecular dynamics computer simulations to understand the formation of ACC. These earlier simulations were mainly for solutions of pure calcium (Ca^{2+}) and carbonate (CO_3^{2-}) ions and mainly focus on the structure investigation of ACC.[29,30] Despite the above studies, details of ACC aggregation (such as the nucleation process, polymerization rate, activation energy, etc.) remain unclear. Moreover, there are many factors that can influence the precipitation of ACC, including the temperature, the solution composition (such as Si, Al), etc., which have been rarely studied before. Comprehending the mechanisms of carbonation on the atomic scale can lay a solid scientific foundation for processes that have hitherto been largely empirically based, thus facilitating the development of new performance-reinforced cementitious materials.

Therefore, to overcome these limitations mentioned above and clarify the carbonation mechanism of carbonation curing cement at the atomic scale, we analyze the carbonation kinetics and calcium carbonate nucleation in the early stage based on molecular dynamics simulations. First, we study how the solution composition (e.g., Si, Al, etc.) affects the carbonation activation energy. Then, in order to reveal the reasons that caused the evolution of polymerization rate and activation energy, we analyze the local stress and charge of atoms.

2. MATERIALS AND METHODS

2.1. Simulated Methodology. We simulate the ACC gel by using the large-scale atomic/molecular massively parallel simulation (LAMMPS) package.[31] It is known that calcium hydroxide solubility in cement concrete pore solution is around 22×10^{-3} mol/L.[32,33] Based on a previous experiment (the adopted Ca^{2+} concentration is 0.2 ×

https://doi.org/10.1021/acssuschemeng.3c07814
ACS Sustainable Chem. Eng. 2024, 12, 10075−10088

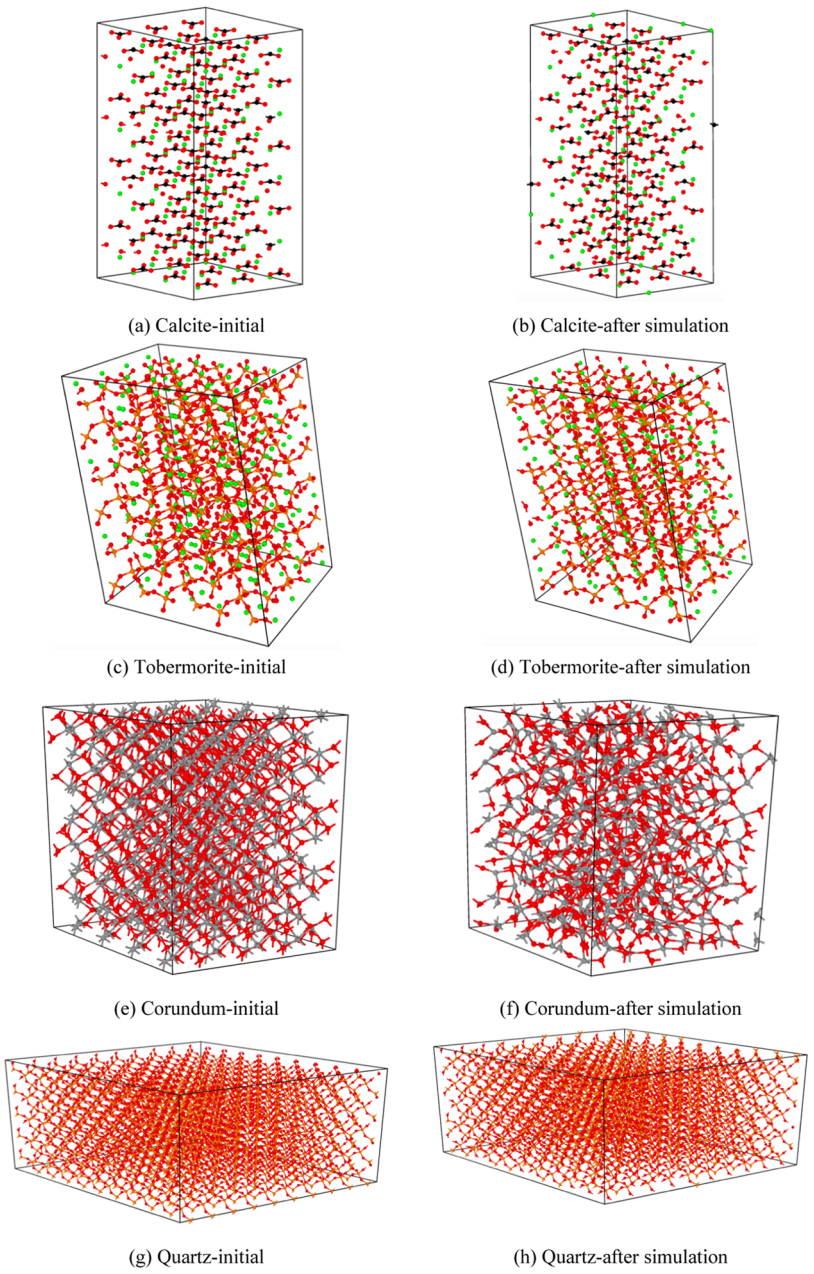

Figure 2. Snapshots of crystals equilibrated at ambient temperature.

10^{-3}–2×10^{-3} mol/L) that investigated the calcium coordination environment[34] and the simulation composition (the Ca^{2+}/H_2O molar ratio is 30/1000) as described in ref 35, we chose the Ca^{2+} concentration as 1.67×10^{-3} mol/L (i.e., the Ca^{2+}/H_2O molar ratio is 30/1000). The CO_3^{2-} concentration is the same as that of the Ca^{2+} concentration to maintain neutrality of the simulation system. It is known that the Si/Ca and Al/Ca ratios of ground granulated blast-furnace slag/fly ash are about 0.4–5.0 and 0–1.0, respectively.[5,36−38] Therefore, in order to investigate the effect of Si/Al components on calcium carbonate nucleation, the adopted Si/Ca ratios are 0, 1, 2, 3, and 4 and the Al/Ca ratios are 0, 0.1, 0.2, 0.3, and 0.4 (when the Si/Ca ratio is fixed at 1) in the simulation system. The specific molecular composition is shown in Table 1.

First, we place separated Ca^{2+}, CO_3^{2-}, H_2O, $Si(OH)_4$, and $Al(OH)_3$ molecules in a 40 Å cubic simulation box randomly without unrealistic atom overlap by using the PACKMOL package,[32,39] and we apply the periodic boundary conditions. The initial configuration snapshots of the simulation systems are shown in Figure 1, where water molecules have been omitted for the sake of clarity. We relax the simulation system in an isothermal–isobaric (NPT) ensemble for 300 ps by using the Nosé–Hoover thermostat and the barostat,[40,41] which is found to be long enough to ensure the convergence of volume, potential energy, and pressure of the whole simulation system. After the relaxation stage, all of the systems are then subjected to various simulation temperatures (300, 325, 350, 400, and 450 K, and the pressure is fixed at 1 atm) in an NPT ensemble for 5 ns. In addition, we use the velocity-Verlet integral algorithm to trace atom motion, and the time step is fixed at 0.25 fs.

2.2. Simulation Force Field. We select the reactive force field (ReaxFF) in this paper because of its ability to bridge the gap between classical molecular dynamics simulations and quantum mechanical calculations. Unlike classical force fields, which model atoms as rigid ions with fixed charges,[42] reactive force fields dynamically adjust atom charges according to the charge equilibration method.[43,44] Atom charges were related to electron affinities, atomic radii, and atomic ionization potentials; therefore, according to each atom's local environment, the reactive force field can adjust the energy terms and can model chemical reactions.[45,46] In addition, the reactive force field can describe the dynamics of chemical bond breaking or formation

https://doi.org/10.1021/acssuschemeng.3c07814
ACS Sustainable Chem. Eng. 2024, 12, 10075−10088

Table 2. Sizes and Densities of Crystals

minerals	items	experimental data	simulated data	error (%)
calcite ($CaCO_3$)	Lx (Å)	15.14	14.72	2.77
	Ly (Å)	13.11	12.67	3.36
	Lz (Å)	34.68	35.59	2.62
	Xy (Å)	−7.57	−7.35	2.91
	Xz (Å)	0	−0.05	
	Yz (Å)	0	0.01	
	density (g/cm^3)	2.61	2.70	3.45
tobermorite (C−S−H)	Lx (Å)	22.32	23.35	4.61
	Ly (Å)	21.91	22.84	4.24
	Lz (Å)	28.13	29.17	3.70
	Xy (Å)	0.01	0.01	0
	Xz (Å)	−1.41	−1.47	4.26
	Yz (Å)	−5.51	−5.69	3.27
	density (g/cm^3)	3.04	2.98	1.97
corundum (α-Al_2O_3)	Lx (Å)	19.02	18.91	0.58
	Ly (Å)	16.47	16.58	0.67
	Lz (Å)	25.97	25.59	1.46
	Xy (Å)	−9.51	−9.43	0.84
	Xz (Å)	0	0.67	
	Yz (Å)	0	−0.28	
	density (g/cm^3)	4.00	4.05	1.25
quartz (SiO_2)	Lx (Å)	49.16	49.17	0.02
	Ly (Å)	42.58	42.59	0.02
	Lz (Å)	27.03	27.10	0.26
	Xy (Å)	−24.58	−24.65	0.28
	Xz (Å)	0	−0.01	
	Yz (Å)	0	0.07	
	density (g/cm^3)	2.64	2.63	0.38

according to the calculation of the interatomic bond order. The atom's local environment determines the interatomic bond order. ReaxFF has been used for aqueous-calcium carbonate systems and the precipitation of early-age calcium−aluminum-silicate-hydrate gel.[32,47−49] The reactive force field system total energy (E_{sys}) can be described by the following equation[50,51]

$$E_{sys} = E_{bond} + E_{Coulomb} + E_{VdWaals} + E_{under} + E_{lp} + E_{over} + E_{tors} + E_{val} + E_{pen} + E_{conj} \quad (5)$$

where E_{bond} and $E_{Coulomb}$ are the short-range bond energy and the Coulomb potential energy, respectively. $E_{VdWaals}$, E_{under}, and E_{lp} represent the van der Waals energy, the under-coordination energy, and the long-range electron pair energy, respectively. E_{over} expresses the overcoordination energy, E_{tors} is the torsion energy, and E_{val} is the valence angle energy. E_{pen} and E_{conj} represent the penalty energy and the conjugation energy, respectively. More details about these 10 energies can be found in refs 50,51.

The parametrization of ReaxFF used in this article is created by integrating the Ca−C/O interactions within the existing Ca/Si/Al/O/H parametrization. The parametrization of ReaxFF can be directly found in previously published references.[47,52] We simulate the calcite ($CaCO_3$), tobermorite (C−S−H), corundum (α-Al_2O_3), and quartz (SiO_2) crystals to test the performance of the created ReaxFF. The initial real structures of these structures are obtained from these references.[53−57] Figure 2 shows snapshots of these crystals equilibrated at ambient temperature. It can be found that the ReaxFF yields a realistic description of the structure of these crystals. The sizes and densities of these crystals are described in Table 2. According to Table 2, the errors between the simulated and experimental values are very small; that is, the sizes and densities of calcite, tobermorite, corundum, and quartz crystals after ReaxFF simulation are in very good agreement with those of experimental data.

Moreover, in order to verify the reliability of the interaction of different groups, we simulate the interfacial interaction energy of Ca^{2+} and CO_3^{2-} with tobermorite (C−S−H), corundum (α-Al_2O_3), and quartz (SiO_2) crystals and compare the results with those calculated by density functional theory (Figure 3). It can be found that the simulation

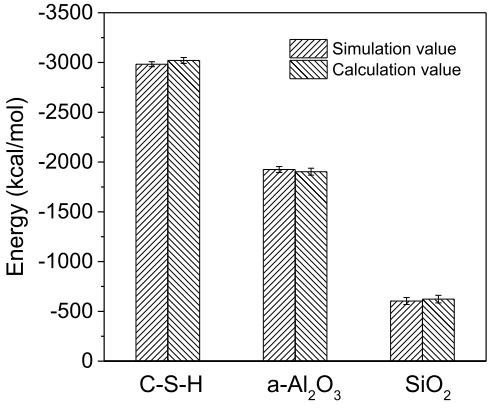

Figure 3. Interfacial interaction energies of Ca^{2+} and CO_3^{2-} with various crystals.

results and calculation results are basically consistent (the errors are 1.27−3.15%). Based on the above analysis, the created ReaxFF is reliable.

2.3. Structural Analysis. The partial coordination number of each atom is calculated via enumerating adjacent atom numbers in the first coordination shell to describe the atomic topological structure of amorphous calcium carbonate gels. In the atomic pair partial pair distribution functions, the minimum distance after the first peak is taken as the atomic pair cutoff. According to the atomic pair cutoff, we can

https://doi.org/10.1021/acssuschemeng.3c07814
ACS Sustainable Chem. Eng. 2024, 12, 10075−10088

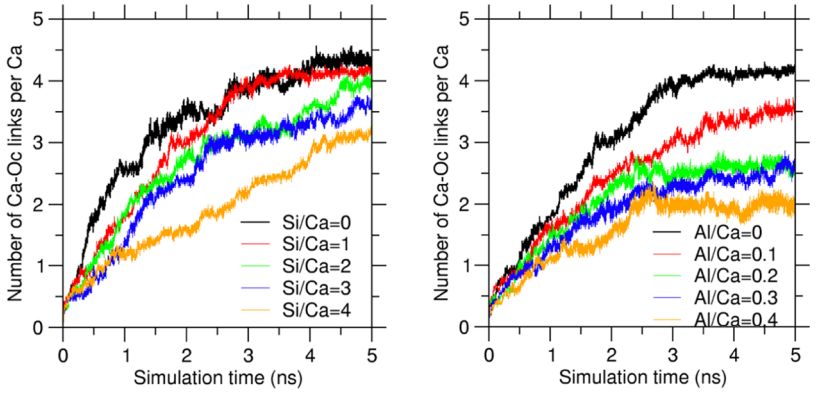

(a) at various Si concentration (b) at various Al concentration

Figure 4. Number of Ca−Oc links per Ca at various Si and Al concentrations when the temperature is 400 K.

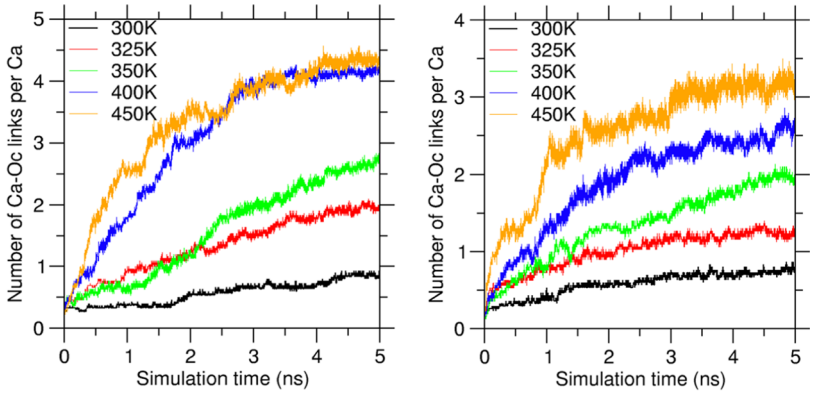

(a) Si/Ca=1 (b) Si/Ca=1, Al/Ca=0.3

Figure 5. Number of Ca−Oc links per Ca at various temperatures.

identify the C−O bond, Ca−O bond, and Ca−C bond in amorphous $CaCO_3$ gel structures. Moreover, we can obtain the network connectivity evolution of the amorphous calcium carbonate gel during gelation and compute the size, number of carbonate clusters, etc. According to the recognition of the C−O bond, Ca−O bond, and Ca−C bond, the calcium carbonate cluster can be identified. Based on the C atoms' number belonging to the carbonate cluster, the size of each cluster can be calculated. The average size is the sum of all clusters' size divided by the total number of clusters, and the largest size is the size of the largest cluster of all clusters. The simulation structure visualization and cluster analysis were carried out by using OVITO software.[58]

2.4. Local Atomic Stress Computation. We use the "stress per atom" concept to evaluate the local instability that exists in the calcium carbonate network; the concept was proposed by Egami.[59,60] In fact, stress is of a macroscopic nature and is therefore difficult to define for a single atom.[61] Nevertheless, an atomic-level stress tensor ($\sigma_i^{\alpha\beta}$), as shown in the following equation, can be defined for each atom according to its contribution to the system dimension.[62]

$$\sigma_i^{\alpha\beta} = 1/V_i \cdot \sum_j r_{ij}^{\alpha} \cdot F_{ij}^{\beta} \quad (6)$$

where V_i is the Voronoi volume of atom i, r_{ij} is the distance between atoms i and j, and F_{ij} is the interatomic force exerted by atom j on atom i. The superscripts α and β refer to the projections of these vectors along the Cartesian directions x, y, or z.[28] Generally speaking, a positive stress here represents that the atom is in a local state of tension, while a negative stress represents that the atom is in a local state of compression. $\sigma_i^{\alpha\beta}$ can capture the local instability in a gel caused by competing interatomic forces[28] and has recently been used to quantify the internal stresses exhibited by mixed-alkali glasses[62−64] and stress-rigid atomic networks.[65]

3. RESULTS AND DISCUSSION

3.1. Network Connectivity Evolution of Calcium Carbonate. In order to disclose the network connectivity evolution of calcium carbonate during its gelation, we study the calcium atom's connectivity. The number evolutions of Ca−Oc (Oc represents the O atom that in CO_3^{2-}) links per Ca (namely, the Ca−Oc partial coordination number) at various Si/Al concentrations and temperatures are shown in Figures 4 and 5, respectively. Figure 4 presents the number of Ca−Oc links per

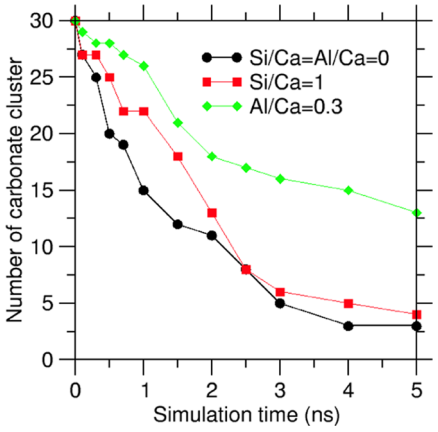

Figure 6. Number of carbonate clusters at different concentrations.

https://doi.org/10.1021/acssuschemeng.3c07814
ACS Sustainable Chem. Eng. 2024, 12, 10075−10088

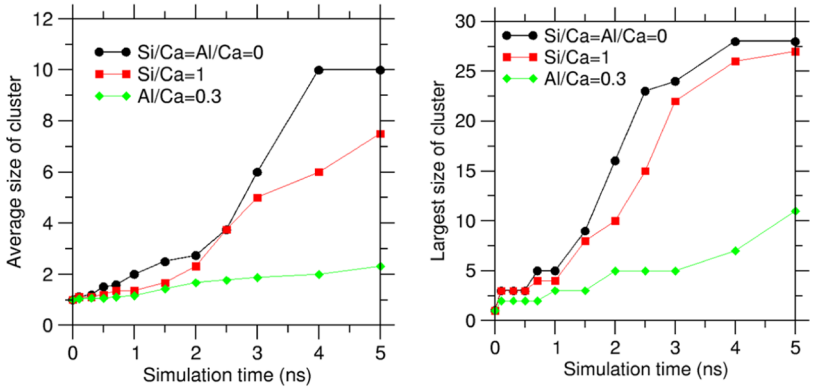

(a) Average size (b) Largest cluster size

Figure 7. Size of carbonate cluster at different concentrations.

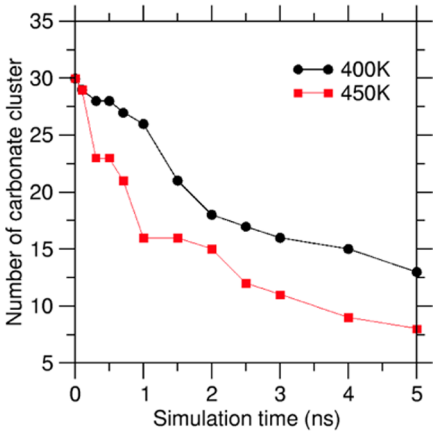

Figure 8. Number of carbonate clusters at different temperatures when the Al/Ca = 0.3.

Ca at various Si and Al concentrations when the temperature is 400 K. It can be found that the Ca−Oc bond number gradually increases with the extension of simulation time, and the Ca−Oc bond number tends to be stable with the prolonging of simulation time. According to Figure 4a,b, the final number of Ca−Oc bonds decreases with the increase of Si/Al concentration, indicating that the final amorphous calcium carbonate gel polymerization degree decreases in the presence of Si/Al. Figure 5 presents the number of Ca−Oc links per Ca at various temperatures when the Si (Si/Ca = 1) or Al (Si/Ca = 1, Al/Ca = 0.3) concentration is fixed. It can be found that temperature has a significant effect on the Ca−Oc bond number. According to Figure 5, a higher temperature can promote the polymerization of calcium carbonate, and the number of Ca−Oc bonds increases with the increase in temperature. The tangent slope of the Ca−Oc bond number curve decreases with the extension of simulation time, indicating that the Ca−Oc bond number tends to be stable.

On the basis of Figures 4 and 5, the formation of Ca−Oc bonds leads to the appearance of carbonate clusters. Figures 6 and 7 show the number and size of carbonate clusters as a function of time at different Si/Al concentrations when the temperature is 400 K. As can be seen, the system consists of numerous isolated small clusters at the beginning. With the prolongation of simulation time, the gel polymerizes gradually, resulting in the decrease of the number of amorphous calcium carbonate gels, accompanied by the increase of the average size and maximum size of calcium carbonate gels. This indicates that the carbonate gelation process is percolative in nature.[28] It can also be found that with the increase of Si/Al concentration, the number of calcium carbonate gels in the system eventually increases and the size becomes smaller, resulting in the formation of calcium carbonate gel clusters with a lower degree of polymerization. It was proven once again that the increase of Al/Si concentration would decrease the polymerization rate and the degree of calcium carbonate gel, which was consistent with

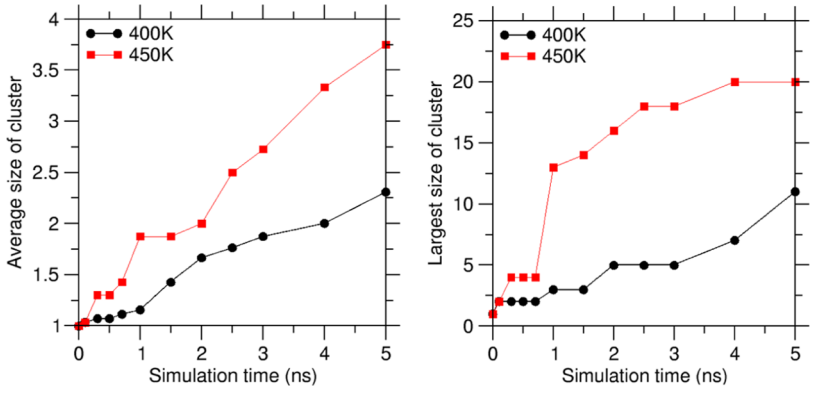

(a) Average size (b) Largest cluster size

Figure 9. Size of carbonate cluster at different temperatures when the Al/Ca = 0.3.

https://doi.org/10.1021/acssuschemeng.3c07814
ACS Sustainable Chem. Eng. 2024, 12, 10075−10088

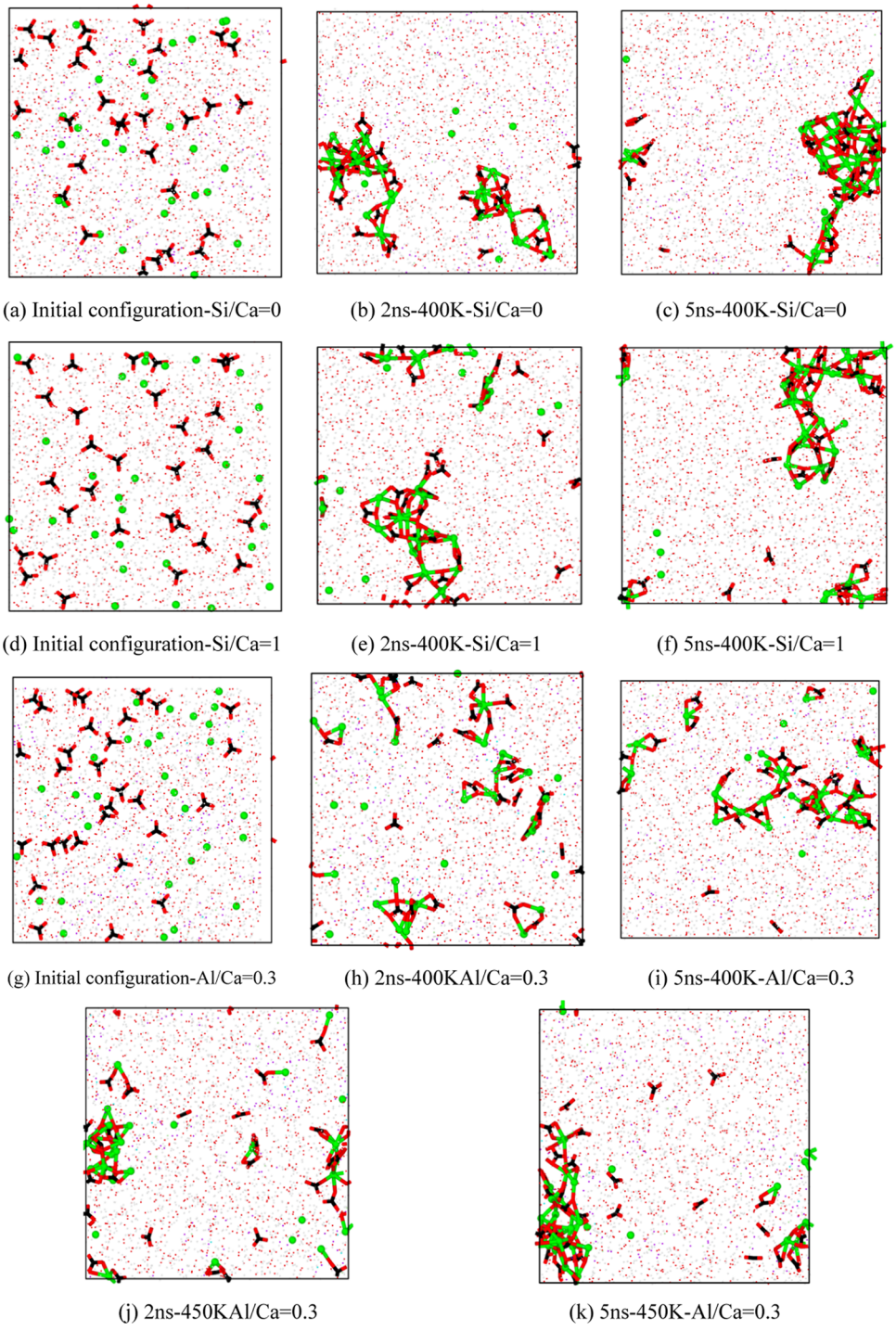

Figure 10. Snapshots of the simulated amorphous $CaCO_3$ system after various nanoseconds of gelation.

the result shown in Figure 4. Figures 8 and 9 show the number and size of carbonate clusters as a function of time at different temperatures when the Al/Ca is 0.3. It can be found that with the increase of temperature, the number of calcium carbonate gels in the final system decreases, and the size becomes larger, resulting in the formation of calcium carbonate gel clusters with a higher degree of polymerization. Therefore, the increase in temperature would increase the polymerization rate and degree of the calcium carbonate gel, which is consistent with the result shown in Figure 5. As shown in Figures 6−9, compared with concentration, the increase in temperature makes the calcium carbonate gel reach a relatively large stable size and a smaller quantity in a very short simulation time. Therefore, the effect of temperature on $CaCO_3$ gel polymerization is greater than that of the concentration.

Figure 10 shows a snapshot of the simulated amorphous $CaCO_3$ system after gelation at different nanoseconds. It is also clear from Figure 10 that Ca^{2+} is isolated at the beginning (Figure 10a,d,g). With the increase of simulation time, CO_3^{2-} clusters are connected by Ca atoms and C−Oc−Ca−Oc−C bonds are formed, leading to the increase of the polymerization degree of the $CaCO_3$ gel. Comparing Figure 10d−i with a−c, the

https://doi.org/10.1021/acssuschemeng.3c07814
ACS Sustainable Chem. Eng. 2024, 12, 10075−10088

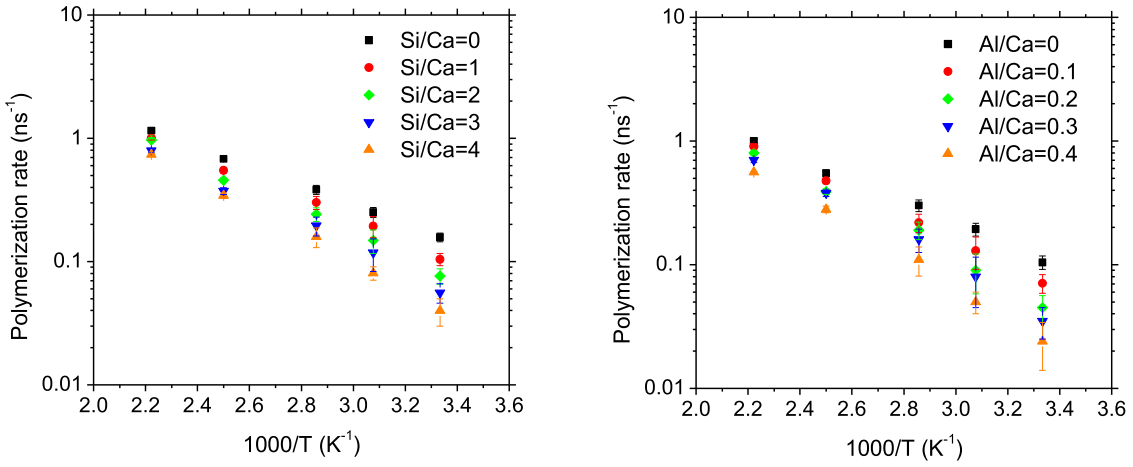

(a) at various Si concentrations (b) at various Al concentrations

Figure 11. Polymerization rate of carbonate at different Si and Al concentrations.

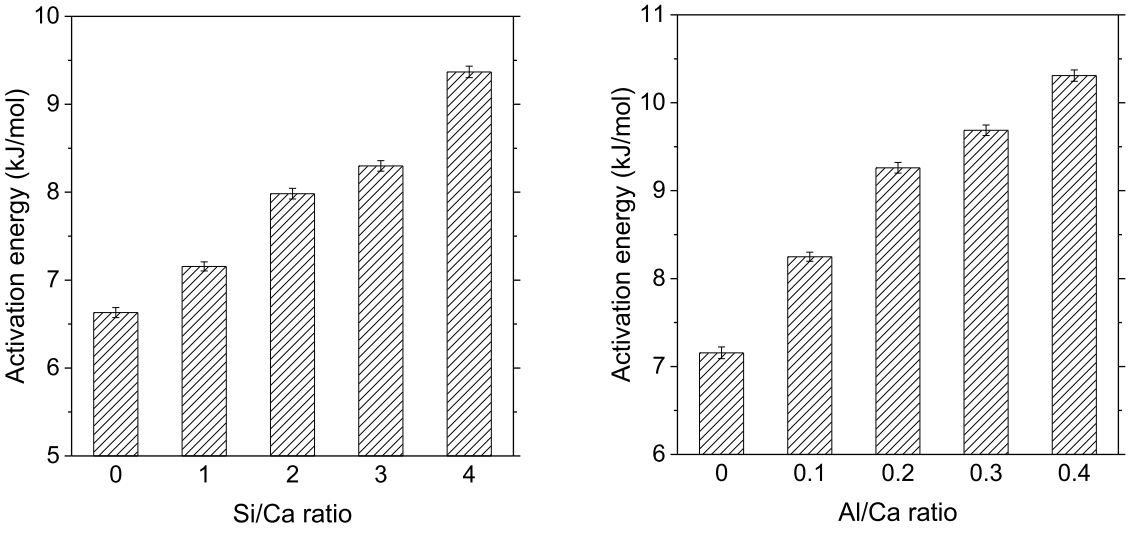

(a) at various Si concentrations (b) at various Al concentrations

Figure 12. Activation energy of carbonate at various concentrations.

addition of Si/Al resulted in a lower polymerization degree of the $CaCO_3$ gel. However, according to Figure 10j,k and b,c, the higher temperature caused a higher calcium carbonate polymerization degree. These phenomena are consistent with the results shown in Figures 4−9.

3.2. Polymerization Kinetics. We investigate the effect of the reaction temperature on $CaCO_3$ gel polymerization in the process of $CaCO_3$ condensation to analyze the reaction kinetics. The number of Ca−Oc bonds was calculated at different Si/Al concentrations and reaction temperatures, and part of the results are presented in Figure 5. We can obtain the polymerization rate according to the fitting of Ca−Oc(t) curves at different temperatures, and the Ca−Oc(t) curves can be fitted by the following function

$$\text{Ca−Oc/Ca}(t) = A[1 - \exp(-kt)] \quad (7)$$

where k and A are the polymerization rate coefficient and the final value of the Ca−Oc/Ca molar ratio at infinite simulation time, respectively. The fitting results of the polymerization rate of calcium carbonate are shown in Figure 11. According to Figure 11, the predicted polymerization rate of calcium carbonate increases with the increase of temperature. Moreover, as shown in Figure 11, regardless of the Si/Al concentrations, the calculated value of polymerization rate K retains an Arrhenius-like dependence on temperature T. It can be found that the polymerization rate of calcium carbonate decreases with higher Si/Al concentrations when the temperature is fixed. The reasons for this phenomenon will be given later. Moreover, according to Figure 11, the Arrhenius curve slopes increase with higher Si/Al concentrations, indicating that the $CaCO_3$ condensation reaction energy barrier increases with the increase of Si/Al concentrations. The activation energy E_A can be calculated based on the following Arrhenius function[66]

$$k(t) = k_0 \cdot \exp(-E_A/RT) \quad (8)$$

where T, k_0, and R are the temperature, the polymerization rate at infinite temperature, and the perfect gas constant, respectively.

https://doi.org/10.1021/acssuschemeng.3c07814
ACS Sustainable Chem. Eng. 2024, 12, 10075−10088

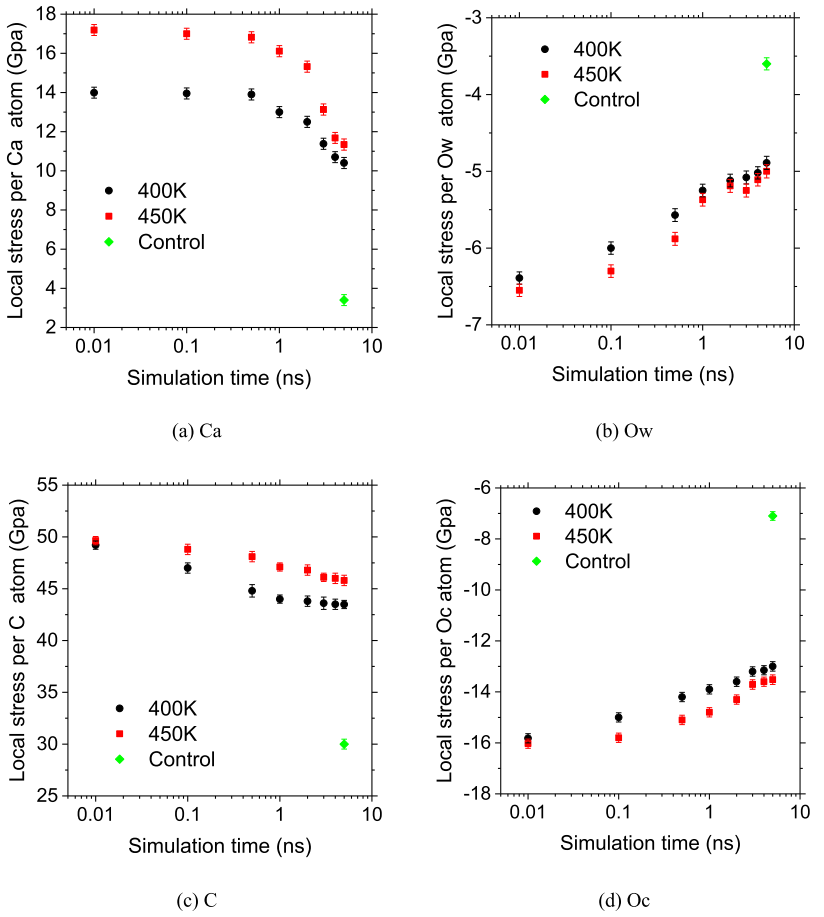

Figure 13. Local stress of Ca, Ow, C, and Oc atoms at various temperatures.

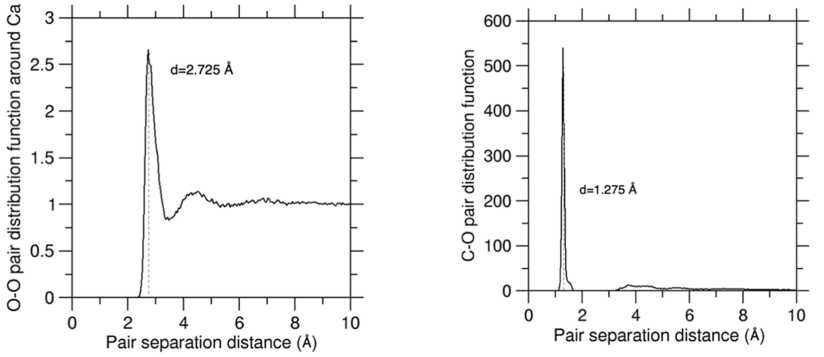

Figure 14. Pair distribution function.

The activation energies of the carbonation reaction obtained under different Si/Al concentrations are shown in Figure 12. The results show that the activation energy of carbonate is 6.63 kJ/mol without the presence of Si/Al, which is in accordance with the experimental data (6−7 kJ/mol).[67,68] Therefore, the ReaxFF molecular dynamics simulation can well-estimate the carbonate condensation energy barrier and, thereby, offers a realistic description of the carbonation kinetics. It can also be found that, in cementitious materials, the activation energies of the carbonation reaction increase with the increase of Si/Al concentrations. The reasons for this phenomenon will be given later.

3.3. Local Stress. The structural local stability of the amorphous calcium carbonate gel is discussed in this part via calculating the local stress of each atom. The Ca, Ow (O atoms belong to H_2O) and C and Oc (O atoms belong to CO_3^{2-} molecules) atoms' local stress evolutions without the presence of Si/Al upon gelation are shown in Figure 13. The control values of Ca, C, and Oc in the figure are the simulated stress values in the pure $CaCO_3$ crystal. The Ow control value is the simulated stress value in pure water. According to Figure 13a,b, it can be found that Ca and Ow atoms are in states of local tension (positive stress) and compression (negative stress), respectively. The origin of the stress state can be considered from the number of adjacent H_2O molecules around the Ca atoms. Figure 14

https://doi.org/10.1021/acssuschemeng.3c07814
ACS Sustainable Chem. Eng. 2024, 12, 10075−10088

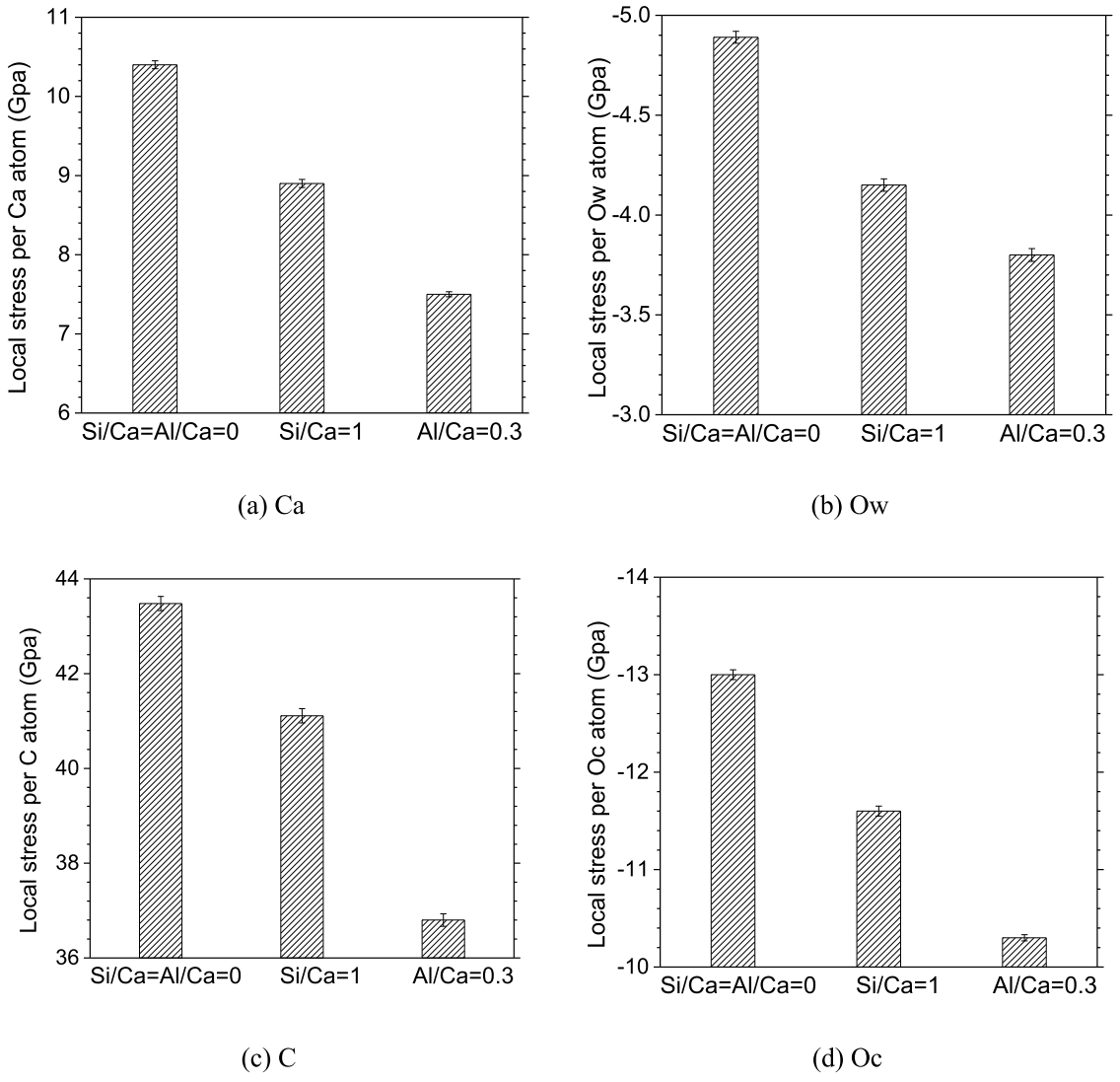

Figure 15. Local stresses of Ca, Ow, C, and Oc atoms at 5 ns of simulation time.

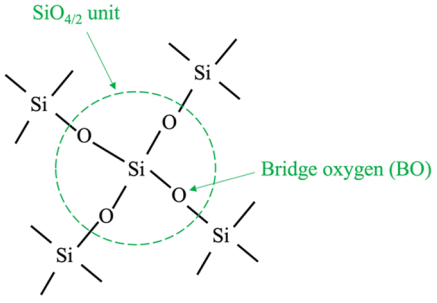

Figure 16. Form of silicon in Portland cement.

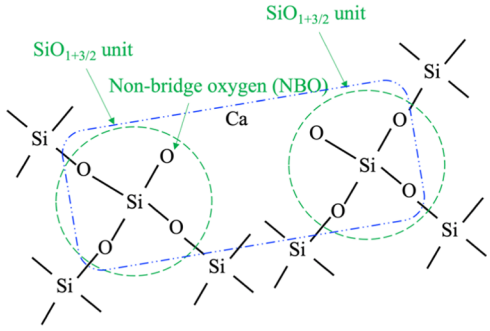

Figure 17. Ca is used as a neutral modifier.

shows the pair distribution functions of O−O around Ca and C−O. Specifically, according to Figure 14a, it can be found that the average O−O distance around Ca^{2+} (2.725 Å, which is in accordance with the experimental data[30]) is smaller than that in bulk water (2.80 Å[69]). This suggests that the distance of adjacent H_2O molecules is smaller than that in bulk water because they are attracted to the central calcium ion. Therefore, due to the existence of repulsive forces, adjacent H_2O molecules appear to be locally compressed. On the contrary, the central Ca atom is stretched due to the repulsion between H_2O molecules, putting the Ca atom in the tension state. The whole CaO_6 polytope is metastable because the local tensile force and compressive force compensate for each other. The tension state of the Ca atom is similar to that of silicate glass, where the Si atom also experiences local tensile stress.[65] Moreover, the Ca atoms' coordination number can be affected by the Ca concentration and the solution pH value,[34] which in turn affect the stress state of Ca atoms. Therefore, how the solution chemistry composition affects the gel precursor stress state deserves further study. Similarly,

https://doi.org/10.1021/acssuschemeng.3c07814
ACS Sustainable Chem. Eng. 2024, 12, 10075−10088

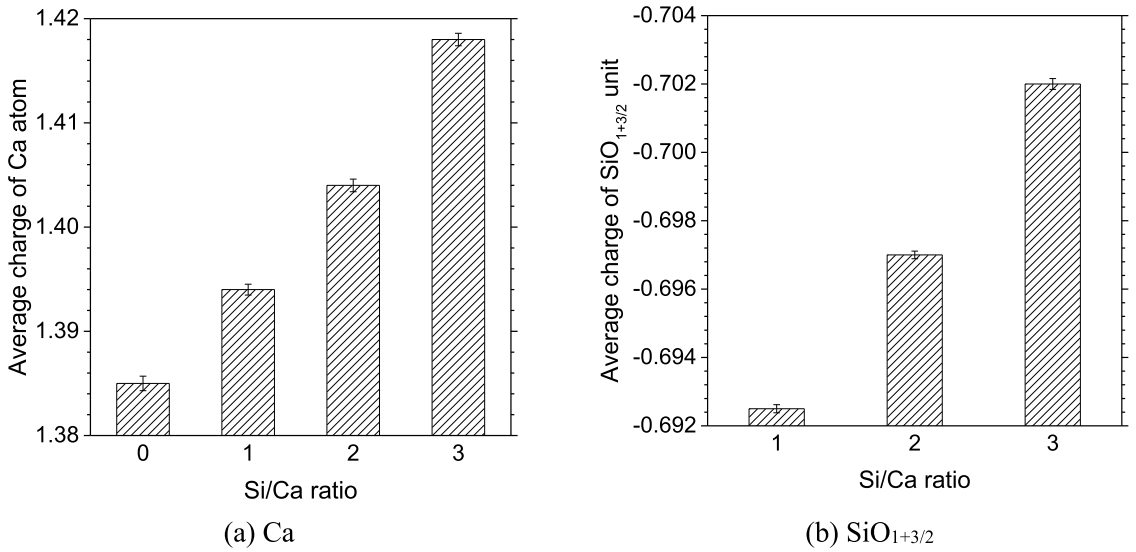

Figure 18. Average charges of Ca and $SiO_{1+3/2}$ at different Si/Ca ratios.

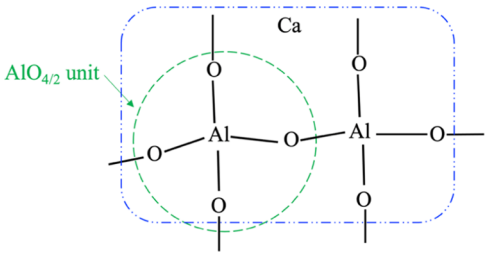

Figure 19. Form of aluminum.

according to Figure 13c,d, C and Oc appear in a stretched and a compressed state, respectively. According to Figure 14b, we observe that the average distance of C−O around the carbon atom is 1.275 Å (such a C−O distance is consistent with the experimental data[30]), which is significantly shorter than the 1.56 Å in the equilibrium state.[70] Therefore, there is obvious mutual Coulomb repulsion between the O atoms around the C atom, leading to the tension state of the C atoms and the compression state of the Oc atoms. The whole CO_3 polytope maintains a metastable state.

These results show that the network locally shows local compression/tensile stresses at the atomic scale due to the significant difference in C and Ca atom coordination numbers even though the whole gel is under zero pressure. Nevertheless, according to Figure 13, this internal stress is gradually released as the $CaCO_3$ gelation progresses. The tensile/compressive stress of each atom decreases gradually and approaches the control value. This indicates that the initial local stress in the system is the driving force of the gelation transition, and the larger the local stress, the greater the polymerization rate of calcium carbonate. It can also be found from Figure 13 that the higher the temperature, the larger the local stress of the atom, which is consistent with the conclusion that the increase of temperature can promote the polymerization rate of the $CaCO_3$ gel as presented in Figure 11. Figure 15 shows the local stresses of Ca, Ow, C, and Oc atoms at 5 ns of simulation time in the presence of Si/Al. As can be seen from the figure, with the addition of Si/Al components, the local stress of each atom decreases. As a

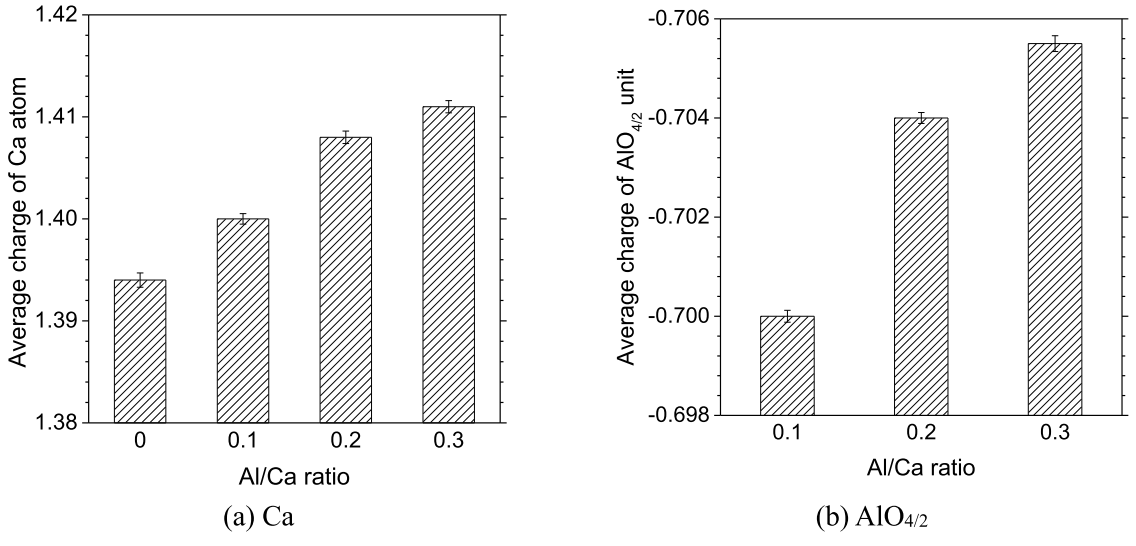

Figure 20. Average charges of Ca and $AlO_{4/2}$ at different Al/Ca ratios.

https://doi.org/10.1021/acssuschemeng.3c07814
ACS Sustainable Chem. Eng. 2024, 12, 10075−10088

result, the $CaCO_3$ gels' polymerization rate decreases, which is also consistent with the result shown in Figure 11.

3.4. Charge Analysis. In order to explain the decrease in the polymerization rate of calcium carbonate and the increase in activation energy caused by Si and Al, we analyze the charges of different groups in this section. According to Figure 1, Si and Al exist in the forms of $Si(OH)_4$ and $Al(OH)_3$, respectively, in the simulated initial configuration. Moreover, the calculated coordination number of Si and Al after polymerization is about 4. Therefore, during the simulation process, the existing form of Si is the same as that of silica gel in cement-based materials, as shown in Figure 16. Silicon oxygen tetrahedron is connected by a bridging oxygen (BO). That is, the BO is shared by two Si atoms, and each silicon is actually neutralized by two oxygens ($SiO_{4/2}$), resulting in the whole $SiO_{4/2}$ unit remaining neutral ($Q(SiO_{4/2}) = (+4) + (4 \times (-2)/2) = 0$). However, as shown in Figure 17, when nonbridged oxygen appears in the silicon−oxygen group, calcium can be used as a network modifier to compensate for the charge imbalance caused by nonbridged oxygen, so that the whole group remains neutral. The charge of the whole group (shown in the blue box in Figure 17) is 0 ($Q(Ca + 2 \times SiO_{1+3/2}) = (+2) + 2 \times (+4) + 6 \times (-2)/2 + 2 \times (-2) = 0$).

Figure 18 shows the simulated charges of the Ca and $SiO_{1+3/2}$ groups at different Si concentrations. It can be found that Ca is positively charged and the $SiO_{1+3/2}$ group is negatively charged. The whole system of the Ca and $SiO_{1+3/2}$ groups remains charge-neutral. Ca ions need to break away from the attraction of $SiO_{1+3/2}$ when they are polymerized with the CO_3 ions. As a result, the polymerization rate of calcium carbonate decreases and the activation energy increases. It can also be seen from Figure 18 that the charge of both Ca and $SiO_{1+3/2}$ groups increases with the increase of Si concentration, which means that the attraction force between Ca and $SiO_{1+3/2}$ increases with the increase of the Si/Ca ratio. Therefore, it is more difficult for Ca ions to break away from the attraction of $SiO_{1+3/2}$. As a result, the activation energy increases with the increase in Si concentration, which is consistent with the result shown in Figure 12a.

The existence form of Al in the simulated system is shown in Figure 19. The $AlO_{4/2}$ group is negatively charged and can attract Ca ions. Calcium can be used as a charge compensator. The group (shown in the blue box in Figure 19) remains electrically neutral ($Q = (+3) \times 2 + (-2) + 6 \times (-2)/2 + (+2) = 0$). Similarly, when Ca ions polymerize with CO_3 ions, they need to break away from the attraction of the $AlO_{4/2}$ group first, which results in the decrease of the polymerization rate and the increase of the activation energy. The simulated charges of the Ca and $AlO_{4/2}$ groups at different Al concentrations are shown in Figure 20. As can be seen from the figure, Ca is positively charged, while the $AlO_{4/2}$ group is negatively charged. The whole system of Ca and $AlO_{4/2}$ groups remains charge neutral. With the increase of the Al/Ca ratio, the charges of both Ca and $AlO_{4/2}$ groups increase, which indicates that the attraction between Ca and $AlO_{4/2}$ increases with the increase of the Al/Ca ratio. As a result, it is more difficult for Ca ions to break away from the attraction of $AlO_{4/2}$, resulting in the increase of the activation energy as shown in Figure 12b.

4. CONCLUSIONS

This paper investigates the effect of Si/Al concentrations on the carbonation kinetics in carbonation curing cementitious materials/wastes, reveals the atomic-scale mechanism of carbonation based on the molecular dynamics simulation, which could promote the mineralization capture, immobilization, and utilization of carbon dioxide, and provides a solid scientific foundation for a process that has so far been largely based on experience, thus facilitating the development of new performance-reinforced and greener cementitious materials. We can obtain the following conclusions according to the simulation results.

(1) In the Si−O system, calcium can be used as a neutral modifier to compensate for the charge imbalance caused by nonbridged oxygen. In the Al−O system, the Ca ions can be attracted by the $AlO_{4/2}$ group and can be used as a charge compensator. These effects cause the increase of the energy barrier of the $CaCO_3$ polymerization.

(2) The CO_3 and CaO_6 polytope precursors show competing internal stress initially even though the entire system is at zero pressure. With the progress of gelation, the local stress of atoms is gradually released, and the tensile/compressive stress of each atom decreases gradually. The local stress of each atom in the system is the driving force of the gelation transition.

(3) The higher the concentration of Si and Al, the higher the atom's local stress and the larger the average charges of Ca, $SiO_{1+3/2}$, and $AlO_{4/2}$, therefore leading to the lower polymerization rate of $CaCO_3$ and the higher activation energy of the carbonate reaction.

(4) Effects of CO_2 concentration, humidity, and pressure on the atomic-scale mechanism of carbonation are still unclear, which will be investigated in the future.

■ ASSOCIATED CONTENT

Data Availability Statement

Data will be made available upon reasonable request.

■ AUTHOR INFORMATION

Corresponding Authors

Ditao Niu − *Department of Civil Engineering, State Key Laboratory of Green Building in Western China, Xi'an University of Architecture and Technology, Xi'an 710055, China*; Email: niuditao@163.com

Xiaojian Gao − *School of Civil Engineering, Harbin Institute of Technology, Harbin 150090, China*; orcid.org/0000-0003-3138-5751; Email: yuqi0421@126.com

Mathieu Bauchy − *Physics of AmoRphous and Inorganic Solids Laboratory (PARISlab), Department of Civil and Environmental Engineering, University of California, Los Angeles, California 90095, United States; Institute for Carbon Management (ICM), University of California, Los Angeles, California 90095, United States*; orcid.org/0000-0003-4600-0631; Email: bauchy@ucla.edu

Authors

Ling Qin − *School of Civil Engineering, Qingdao University of Technology, Qingdao 266033, China; Post-doctoral Mobile Stations of Civil engineering, Xi'an University of Architecture and Technology, Xi'an 710055, China; Qingdao Qingjian New Material Group Co., Ltd., Qingdao 266108, China; Physics of AmoRphous and Inorganic Solids Laboratory (PARISlab), Department of Civil and Environmental Engineering, University of California, Los Angeles, California 90095, United States*

Qijie Xie − *School of Civil Engineering, Qingdao University of Technology, Qingdao 266033, China*

https://doi.org/10.1021/acssuschemeng.3c07814
ACS Sustainable Chem. Eng. 2024, 12, 10075−10088

Jiuwen Bao − *School of Civil Engineering, Qingdao University of Technology, Qingdao 266033, China*
Gaurav Sant − *Institute for Carbon Management (ICM), University of California, Los Angeles, California 90095, United States;* orcid.org/0000-0002-1124-5498
Tiefeng Chen − *School of Civil Engineering, Harbin Institute of Technology, Harbin 150090, China*
Peng Zhang − *School of Civil Engineering, Qingdao University of Technology, Qingdao 266033, China*

Complete contact information is available at: https://pubs.acs.org/10.1021/acssuschemeng.3c07814

Author Contributions

L.Q.: writing—original draft; investigation; writing—review and editing; methodology. Q.X.: writing—review and editing. J.B.: writing—review and editing. G.S.: writing—review and editing. T.C.: writing—review and editing. P.Z.: funding acquisition; writing—review and editing. D.N.: writing—review and editing. X.G.: writing—review and editing; funding acquisition. M.B.: Writing—review and editing; funding acquisition; supervision.

Notes

The authors declare no competing financial interest.

■ ACKNOWLEDGMENTS

This research was supported by the National Key Research and Development Program of China (2021YFB2600704), the National Natural Science Foundation of China (52208260, U23A20661), the Natural Science Foundation of Shandong province (ZR2022QE002), the National Science Foundation (DMREF-1922167), the National Postdoctoral Fund Project (2023MD734207), and all of LAMMPS developers at Sandia National Laboratories and Temple University.

■ REFERENCES

(1) Wang, C.; Chen, J.; Zou, J. Decomposition of energy-related CO_2 emission in China: 1957−2000. *Energy* **2005**, *30*, 73−83.
(2) Biernacki, J. J.; Bullard, J. W.; Sant, G.; Brown, K.; Glasser, F. P.; Prater, T.; et al. Cements in the 21st century: challenges, perspectives, and opportunities. *J. Am. Ceram. Soc.* **2017**, *100*, 2746−2773.
(3) Shi, C.; Jiménez, A. F.; Palomo, A. New cements for the 21st century: the pursuit of an alternative to Portland cement. *Cem. Concr. Res.* **2011**, *41*, 750−763.
(4) Schneider, M.; Romer, M.; Tschudin, M.; Bolio, H. Sustainable cement production—present and future. *Cem. Concr. Res.* **2011**, *41*, 642−650.
(5) Wei, Z.; Wang, B.; Falzone, G.; et al. Clinkering-free cementation by fly ash carbonation. *J. CO_2 Util.* **2018**, *23*, 117−127.
(6) Habert, G.; Miller, S. A.; John, V. M.; Provis, J.; Scrivener, K. L.; et al. Environmental impacts and decarbonization strategies in the cement and concrete industries. *Nat. Rev. Earth Environ.* **2020**, *1*, 559−573.
(7) Vance, K.; Falzone, G.; Pignatelli, I.; Bauchy, M.; Balonis, M.; Sant, G. Direct carbonation of $Ca(OH)_2$ using liquid and supercritical CO_2: implications for carbon-neutral cementation. *Ind. Eng. Chem. Res.* **2015**, *54*, 8908−8918.
(8) Giergiczny, Z.; Król, A.; Wandoch, K.; et al. Performance of Concrete with Low CO_2 Emission. *Energies* **2020**, *13*, No. 4328, DOI: 10.3390/en13174328.
(9) Hemalatha, T.; Ramaswamy, A. A review on fly ash characteristics—towards promoting high volume utilization in developing sustainable concrete. *J. Cleaner Prod.* **2017**, *147*, 546−559.
(10) Chatterjee, A.; Sui, T. Alternative fuels—Effects on clinker process and properties. *Cem. Conr. Res.* **2019**, *123*, No. 105777.
(11) Kaliyavaradhan, S. K.; Ling, T. C. Potential of CO_2 sequestration through construction and demolition (C&D) waste—an overview. *J. CO_2 Util.* **2017**, *20*, 234−242.
(12) Qin, L.; Mao, X.; Gao, X.; Zhang, P.; Li, Q.; Chen, T.; Cui, Y. Influence of CO_2 curing and autoclaved aerated concrete powder on sulfate attack of cement paste at low temperature. *J. Mater. Civil Eng.* **2023**, *35*, No. 04023059.
(13) Zhan, B.; Poon, C. S.; Liu, Q.; Kou, S.; Shi, C. Experimental study on CO_2 curing for enhancement of recycled aggregate properties. *Constr. Build. Mater.* **2014**, *67*, 3−7.
(14) Monkman, S.; MacDonald, M. On carbon dioxide utilization as a means to improve the sustainability of ready-mixed concrete. *J. Cleaner Prod.* **2017**, *167*, 365−375.
(15) Qian, X.; Wang, J.; Fang, Y.; Wang, L. Carbon dioxide as an admixture for better performance of OPC-based concrete. *J. CO_2 Util.* **2018**, *25*, 31−38.
(16) Monkman, S.; MacDonald, M.; Hooton, R. D.; Sandberg, P. Properties and durability of concrete produced using CO_2 as an accelerating admixture. *Cem. Concr. Compos.* **2016**, *74*, 218−224.
(17) Qin, L.; Mao, X.; Gao, X.; Zhang, P.; Chen, T.; Li, Q.; Cui, Y. Performance degradation of CO_2 cured cement-coal gangue pastes with low-temperature sulfate solution immersion. *Case Stud. Constr. Mater.* **2022**, *17*, No. e01199.
(18) Qin, L.; Gao, X.; Su, A.; Li, Q. Effect of carbonation curing on sulfate resistance of cement-coal gangue paste. *J. Cleaner Prod.* **2021**, *278*, No. 123897.
(19) Zhang, D.; Liu, T.; Shao, Y. Weathering carbonation behavior of concrete subject to early-age carbonation curing. *J. Mater. Civil Eng.* **2020**, *32*, No. 04020038.
(20) Liu, Z.; Meng, W. Fundamental understanding of carbonation curing and durability of carbonation-cured cement-based composites: A review. *J. CO_2 Util.* **2021**, *44*, No. 101428.
(21) Lim, T.; Ellis, B. R.; Skerlos, S. J. Mitigating CO_2 emissions of concrete manufacturing through CO_2-enabled binder reduction. *Environ. Res. Lett.* **2019**, *14*, No. 114014.
(22) Young, J. F.; Berger, R.; Breese, J. Accelerated curing of compacted calcium silicate mortars on exposure to CO_2. *J. Am. Ceram. Soc.* **1974**, *57*, 394−397.
(23) Zhang, D.; Ghouleh, Z.; Shao, Y. Review on carbonation curing of cement-based materials. *J. CO_2 Util.* **2017**, *21*, 119−131.
(24) Qin, L.; Gao, X. Properties of coal gangue-Portland cement mixture with carbonation. *Fuel* **2019**, *245*, 1−12, DOI: 10.1016/j.fuel.2019.02.067.
(25) Qin, L.; Gao, X. Recycling of waste autoclaved aerated concrete powder in Portland cement by accelerated carbonation. *Waste Manage.* **2019**, *89*, 254−264.
(26) Qin, L.; Gao, X.; Chen, T. Influence of mineral admixtures on carbonation curing of cement paste. *Constr. Build. Mater.* **2019**, *212*, 653−662.
(27) Wang, Y.-W.; Kim, Y.; Stephens, C.; Meldrum, F.; Christenson, H. In situ study of the precipitation and crystallization of amorphous calcium carbonate (ACC). *Cryst. Growth Des.* **2012**, *12*, 1212−1217.
(28) Zhou, Q.; Du, T.; Guo, L.; Sant, G.; Bauchy, M. Role of internal stress in the early-stage nucleation of amorphous calcium carbonate gels. *Appl. Sci.* **2020**, *10*, No. 4359, DOI: 10.3390/app10124359.
(29) Quigley, D.; Rodger, P. M. Free energy and structure of calcium carbonate nanoparticles during early stages of crystallization. *J. Chem. Phys.* **2008**, *128*, No. 221101, DOI: 10.1063/1.2940322.
(30) Raiteri, P.; Jale, J. D. Water is the key to nonclassical nucleation of amorphous calcium carbonate. *J. Am. Chem. Soc.* **2010**, *132*, 17623−17634.
(31) https://www.lammps.org/.
(32) Qin, L.; Mao, X.; Cui, Y.; Bao, J.; Sant, G.; Chen, T.; Zhang, P.; Gao, X.; Bauchy, M. New insights into the early stage nucleation of calcium carbonate gels by reactive molecular dynamics simulations. *J. Chem. Phys.* **2022**, *157*, No. 234501.
(33) Pallagi, A.; Tasi, Á.; Gácsi, A. The solubility of $Ca(OH)_2$ in extremely concentrated NaOH solutions at 25°C. *Cent. Eur. J. Chem.* **2012**, *10*, 332−337.

(34) Avaro, J.; Moon, E. M.; Rose, J.; Rose, A. L. Calcium coordination environment in precursor species to calcium carbonate mineral formation. *Geochim. Cosmochim. Acta* **2019**, *259*, 344−357.
(35) Smeets, P. J. M.; Finney, A. R.; Habraken, W.; et al. A classical view on nonclassical nucleation. *Proc. Natl. Acad. Sci. U.S.A.* **2017**, *114*, E7882−E7890.
(36) Richardson, I. G.; Brough, A. R.; Groves, G. W.; Dobson, C. M. The characterization of hardened alkali-activated blast-furnace slag pastes and the nature of the calcium silicate hydrate (c-s-h) phase. *Cem. Concr. Res.* **1994**, *24*, 813−829.
(37) Richardson, I. G.; Groves, G. W. The structure of calcium silicate hydrate phases present in hardened pastes of white Portland cement/blast-furnace slag blends. *J. Mater. Sci.* **1997**, *32*, 4793−4802.
(38) Manzano, H.; Dolado, J. S.; Griebel, M.; Hamaekers, J. A molecular dynamics study of the aluminosilicate chains structure in al-rich calcium silicate hydrated (c-s-h) gels. *Phys. Status Solidi A* **2008**, *205*, 1324−1329.
(39) Martínez, L.; Andrade, R. A.; Birgin, E. G.; Martínez, J. M. PACKMOL: A package for building initial configurations for molecular dynamics simulations. *J. Comput. Chem.* **2009**, *30*, 2157−2164.
(40) Shinoda, W.; Shiga, M.; Mikami, M. Rapid estimation of elastic constants by molecular dynamics simulation under constant stress. *Phys. Rev. B* **2004**, *69*, No. 134103.
(41) Tuckerman, M. E.; Alejandre, J.; López-Rendón, R.; Jochim, A. L.; Martyna, G. J. A liouville-operator derived measure-preserving integrator for molecular dynamics simulations in the isothermal−isobaric ensemble. *J. Phys. A: Math. Gen.* **2006**, *39*, 5629−5651.
(42) Raiteri, P.; Demichelis, R.; Gale, J. D. Thermodynamically consistent force field for molecular dynamics simulations of alkaline-earth carbonates and their aqueous speciation. *J. Phys. Chem. C* **2015**, *119*, 24447−24458.
(43) Rappe, A. K.; Goddard, W. A. Charge equilibration for molecular dynamics simulations. *J. Phys. Chem. A* **1991**, *95*, 3358−3363.
(44) Demiralp, E.; Çağin, T.; Goddard, W. A. Morse stretch potential charge equilibrium force field for ceramics: Application to the quartz-stishovite phase transition and to silica glass. *Phys. Rev. lett.* **1999**, *82*, 1708−1711.
(45) Yu, Y.; Wang, B.; Wang, M.; Sant, G.; Bauchy, M. Revisiting silica with ReaxFF: towards improved predictions of glass structure and properties via reactive molecular dynamics. *J. Non-Cryst. Solids* **2016**, *443*, 148−154.
(46) Yu, Y.; Wang, B.; Wang, M.; Sant, G.; Bauchy, M. Reactive molecular dynamics simulations of sodium silicate glasses—toward an improved understanding of the structure. *Int. J. Appl. Glass Sci.* **2017**, *8*, 276−284.
(47) Gale, J. D.; Raiteri, P.; Van Duin, A. C. A reactive force field for aqueous-calcium carbonate systems. *Phys. Chem. Chem. Phys.* **2011**, *13*, 16666−16679.
(48) Dasgupta, N.; Chen, C.; van Duin, A. C. T. Development and application of ReaxFF methodology for understanding the chemical dynamics of metal carbonates in aqueous solutions. *Phys. Chem. Chem. Phys.* **2022**, *24*, 3322−3337, DOI: 10.1039/D1CP04790F.
(49) Zhao, C.; Liu, H.; Guo, L.; Bauchy, M.; et al. Precipitation of calcium−alumino−silicate−hydrate gels:the role of the internal stress. *J. Chem. Phys.* **2020**, *153*, No. 014501.
(50) van Duin, A. C. T.; Strachan, A.; Stewman, S.; Zhang, Q.; Xu, X.; Goddard, W. A. ReaxFF SiO reactive force field for silicon and silicon oxide systems. *J. Phys. Chem. A* **2003**, *107*, 3803−3811.
(51) van Duin, A. C. T.; Dasgupta, S.; Lorant, F.; Goddard, W. A. ReaxFF: a reactive force field for hydrocarbons. *J. Phys. Chem. A* **2001**, *105*, 9396−9409.
(52) Du, T.; Li, H.; Sant, G.; Bauchy, M. New Insights into the sol−gel condensation of silica by reactive molecular dynamics simulations. *J. Chem. Phys.* **2018**, *148*, No. 234504.
(53) Graf, D. L. Crystallographic tables for the rhombohedral carbonates. *Am. Mineral.: J. Earth Planet. Mater.* **1961**, *46*, 1283−1316.
(54) Ishizawa, N.; Miyata, T.; Minato, I.; Marumo, F.; Iwai, S. A structural investigation of α-Al_2O_3 at 2170 K. *Acta Crystallogr., Sect. B: Struct. Crystallogr. Cryst. Chem.* **1980**, *36*, 228−230.
(55) De la Torre, Á. G.; Vera, R.; Cuberos, A.; Aranda, M. Crystal structure of low magnesium-content alite: application to rietveld quantitative phase analysis. *Cem. Concr. Res.* **2008**, *38*, 1261−1269.
(56) Weidner, D. J. Structure and elastic properties of quartz at pressure. *Am. Mineral.* **1980**, *65*, 920−930.
(57) Merlino, S.; Bonaccorsi, E.; Armbruster, T. The real structures of clinotobermorite and tobermorite 9? *Eur. J. Mineral.* **2000**, *12*, 411−429.
(58) Stukowski, A. Visualization and analysis of atomistic simulation data with OVITO—the open visualization tool. *Modell. Simul. Mater. Sci. Eng.* **2010**, *18*, 2154−2162.
(59) Vitek, V.; Egami, T. Atomic level stresses in solids and liquids. *Phys. Status Solidi B* **1987**, *144*, 145−156.
(60) Egami, T. Atomic level stresses. *Prog. Mater. Sci.* **2011**, *56*, 637−653.
(61) Thompson, A. P.; Plimpton, S. J.; Mattson, W. General formulation of pressure and stress tensor for arbitrary many-body interaction potentials under periodic boundary conditions. *J. Chem. Phys.* **2009**, *131*, No. 154107.
(62) Yu, Y.; Wang, M.; Krishnan, N. M. A.; Smedskjaer, M. M.; Vargheese, K. D.; Mauro, J. C.; Balonis, M.; Bauchy, M. Hardness of silicate glasses: Atomic-scale origin of the mixed modifier effect. *J. Non-Cryst. Solids.* **2018**, *489*, 16−21, DOI: 10.1016/j.jnoncrysol.2018.03.015.
(63) Yu, Y.; Wang, M.; Smedskjaer, M. M.; Mauro, J. C.; Sant, G.; Bauchy, M. Thermometer effect: origin of the mixed alkali effect in glass relaxation. *Phys. Rev. Lett.* **2017**, *119*, No. 095501.
(64) Yu, Y.; Mauro, J. C.; Bauchy, M. Stretched exponential relaxation of glasses: Origin of the mixed-alkali effect. *Am. Ceram. Soc. Bull.* **2017**, *96*, 34−36.
(65) Li, X.; Song, W.; Smedskjaer, M. M.; Mauro, J. C.; Bauchy, M. Quantifying the internal stress in over-constrained glasses by molecular dynamics simulations. *J. Non-Cryst. Solids: X* **2019**, *1*, No. 100013.
(66) Giap, S. G. The hidden property of Arrhenius-type relationship: viscosity as a function of temperature. *J. Phys. Sci.* **2010**, *21*, 29−39.
(67) Montes-Hernandez, G.; Chiriac, R.; Toche, F.; Renard, F. Gas-solid carbonation of $Ca(OH)_2$ and CaO particles under non-isothermal and isothermal conditions by using a thermogravimetric analyzer: Implications for CO_2 capture. *Int. J. Greenhouse Gas Control* **2012**, *11*, 172−180.
(68) Vance, K.; Falzone, G.; Pignatelli, I.; et al. Direct carbonation of $Ca(OH)_2$ using liquid and supercritical CO_2:implications for carbon-neutral cementation. *Ind. Eng. Chem. Res.* **2015**, *54*, 8908−8918.
(69) Mähler, J.; Persson, I. A Study of the hydration of the alkali metal ions in aqueous solution. *Inorg. Chem.* **2012**, *51*, 425−438.
(70) Shannon, R. D. Revised effective ionic radii and systematic studies of interatomic distances in halides and chalcogenides. *Acta Crystallogr. Sect. A* **1976**, *32*, 751−767.